Holocene tephrochronology of Kerguelen Archipelago, Subantarctic Indian Ocean

Fabien Arnaud[1], Pierre Sabatier[1], Anouk Leloup[1], Aymerick Servettaz[1,2], Bertrand Moine [3], Anne-Lise Develle[1], Stéphane Guédron[4], Vincent Perrot[4], Cécile Pignol[1], Jérôme Poulenard[1], Bernard Fanget[1], Emmanuel Malet[1], Eivind Storen[5], Jean-Louis Reyss[1,2], Nicolas Le Viavan[6], Katrien Heirman[7], Marc De Batist[7], Elisabeth Michel[2], Jacques-Louis de Beaulieu[8], Nathalie Van der Putten[2], Jostein Bakke[5]

1) Univ. Grenoble Alpes, Univ. Savoie Mont Blanc, CNRS, EDYTEM, 73000 Chambéry, France
2) Laboratoire des Sciences du Climat et de l'Environnement (LSCE), CEA, CNRS, 91 Gif-sur-Yvette3 : Laboratoire Magmas et Volcans, Université Jean Monnet, CNRS, 42023 Saint-Etienne France
4) Univ. Grenoble Alpes, Univ. Savoie Mont Blanc, CNRS, IRD, IFSTTAR, ISTerre, 38000 Grenoble, FranceInstitut des Sciences de la Terre (ISTerre), Université Grenoble Alpes, CNRS, Grenoble, France
5) Department of Earth Science and Bjerknes Centre for Climate Research, University of Bergen, Allégaten 41, 5007 Bergen, Norway
6) Institut Paul-Emile Victor, 29280, Plouzané, France
7) Renard Centre of Marine Geology, Department of Geology, Ghent University, Krijgslaan 281 S8, B-9000 Ghent, Belgium
8) TNO – Geological Survey of the Netherlands, Princetonlaan 6, NL-3584 CB Utrecht, Netherlands
9) Institut Méditerranéen de Biodiversité et d'Ecologie marine et occidentale (IMBE), Aix-Marseille Université, CNRS, 13545 Aix en Provence, France
10) Department of Earth Sciences, VU University Amsterdam, De Boelelaan 1085, 1081 HV, Amsterdam, the Netherlands

Abstract

Up to now, no geochemical or geochronological data has been published about Holocene volcanic activity on the Kerguelen Archipelago. Here we present the first continuous Holocene chronology of volcanic eruptions on the archipelago. We compared sedimentological, geochronological and geochemical data from two lake sediment cores taken in two different depocenters of Lake Armor, located ca. 70 km away from the archipelago's main volcanic area. This allowed us to confidently assign the pumice- and ash-rich layers that are interbedded in the lake sediments to distinct volcanic eruptions. Eight main and 3 minor eruptions were thus documented and dated, among which the youngest occurred during the Middle Ages, in AD 1020 +/- 58. The oldest eruption is also by far the strongest and deposited, more than 1.2 m of up to 3 cm-large pumices in Lake Armor area. The new tephrostratigraphy presented here may serve as a tool to synchronise paleoenvironmental records from Kerguelen as well as marine records from he Kerguelen rise and beyond. areas.

Keywords

Kerguelen, Lake sediments, Tephrostratigraphy, Subantarctic Indian Ocean

Introduction

Kerguelen Archipelago is located in the sub-Antarctic Indian Ocean, several thousands of kilometres away from any continental landmass (Fig. 1). Its location in the vicinity of the current position of the subpolar front and within the southern westerly wind belt, makes if particularly sensitive to global climate change and thus a potential key place for climate reconstruction. Moreover, high-quality, millennial-long scale palaeoecological and paleoclimatological records are still scarce in this part of the world (Oppedal et al., 2018; Saunders et al., 2018; Shulmeister et al., 2004; van der Bilt et al., 2017; Van der Putten et al., 2004, 2008, 2015). This makes Kerguelen a potential key target for paleoenvironmental reconstructions such as changes in oceanic and atmospheric circulation patterns (e.g. Sijp and England, 2009). Kerguelen's main island and its dozens of surrounding isles and islets, host a myriad of lakes and peatbogs, holding a great potential for reconstructions of past climate and environment (Arnaud et al., 2016). Lakes in particular are numerous and present a great variety of settings, ranging from small ponds suitable for aDNA ((Ficetola et al., 2018) and biomarker palaeothermometry (e.g. Peterse et al., 2014), alpine proglacial lakes that may serve for glacier reconstruction (Dahl et al., 2003; L. T. Oppedal et al., 2018) to fjord-type lakes with large catchments and river systems suitable for paleohydrological reconstructions (Arnaud et al., 2012; Debret et al., 2010; Wessels, 1998). Paleoenvironmental information is particularly robust when such multi-proxy records from different types of lakes are comparable within a precise chronological framework. The restricted vegetation and, in consequence, paucity of terrestrial organic carbon in alpine lake sediments makes the use of radiocarbon dating challenging. It is hence crucial for further studies to establish a common time-scale with ubiquitous tie markers identifiable at least at the archipelago scale. The volcanic nature of the Kerguelen Archipelago, together with indications of recent volcanic activity, makes it possible to use tephrostratigraphy to construct such a chronological framework for correlating different proxy-records (Fontijn et al., 2016; Oppedal et al., 2018).

Present-day geothermal activity is evidenced by the presence of fumaroles and hot springs on the Rallier Du Baty Peninsula (Fig. 1), in the South-Western part of Kerguelen's main island. Indeed, the most recent evidence of volcanism was found on the Rallier du Baty Peninsula and dated at 26 ± 3 ka BP (Gagnevin et al., 2003). Field observations suggest the existence of more recent volcanic activity as ash and pumice layers of variable thickness were found in peat deposits (Roche-Bellair, 1976; Van der Putten et al., 2015). However, until now no Holocene volcanic deposits have been directly dated and published except for a trachyte of the "Dôme Carva" volcano complex, which was Ar/Ar-dated at about 10 ka (Ethien et al., 2003).

Here, we present results from the study of two sediment cores from Lake Armor, on Kerguelen's main island (Fig. 1). Both cores contain several well-marked pumice or ash layers. We particularly address the question whether the ash layers are the result of a contemporaneous volcanic eruption or of post-eruptional remobilisation and re-deposition. Every volcanic event deposit is given an age based on radiocarbon dating and the individual layers are geochemically characterised resulting in the first Holocene tephrostratigraphic framework from the Kerguelen Archipelago.

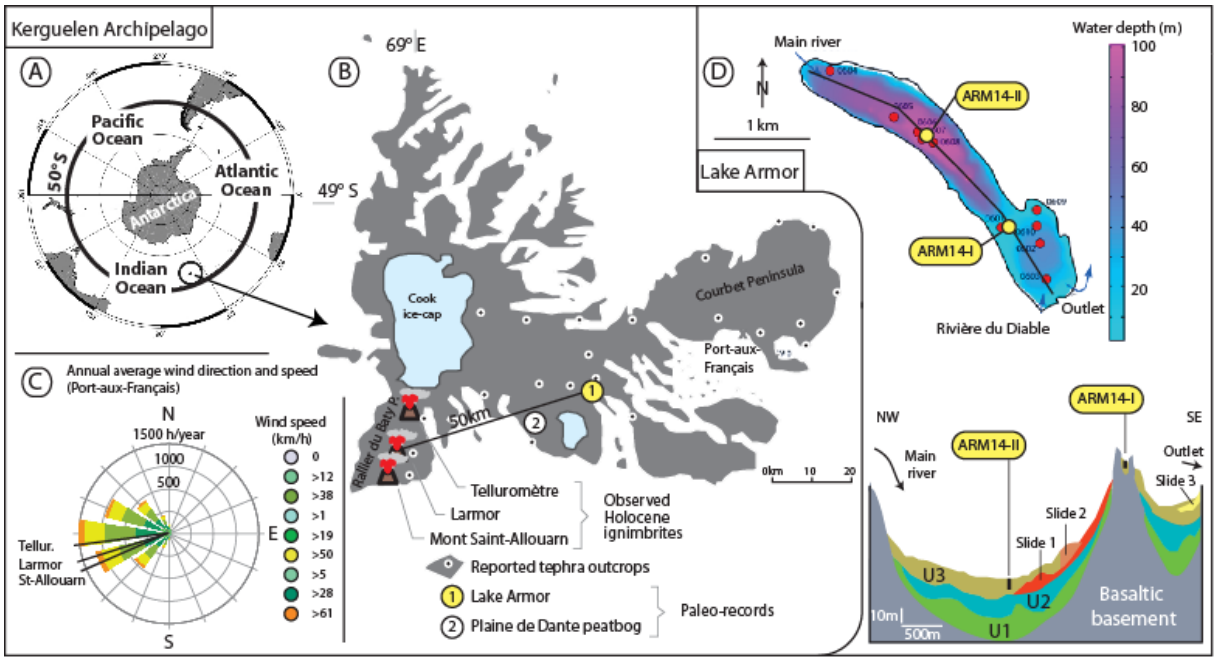

Fig. 1 A: The Southern Ocean with a circle marking the location of the Archipelago Kerguelen located at 49°S in the sub-Antarctic sector of the Indian Ocean. B: Kerguelen with the main geographical features, the location of the Cook Ice cap and the major volcanos in the south. C: Dominant wind speed and direction, recorded at the French research station at Port-aux-Français. D: Lake sediment core locations in Lake Armor, plotted on a bathymetry map and a simplified seismic profile, based on (Heirman et al., 2012).

2. Setting, material and methods

The main island of the Kerguelen Archipelago has a surface area of *ca*. 7215 km^2. It is the emerged part of the Kerguelen-Gaussberg Oceanic Plateau, which was formed by a series of giant basaltic eruptions ca. 40 Ma ago when the SE Indian Ridge (SEIR) overlapped the Kerguelen mantle plume. Since 25 Ma the SEIR migrated to the north but hot spot-type volcanism remained active, due the persistence of the mantle plume (Ethien et al., 2003). Through time, the magmatic activity decreased leading to differentiation processes and a shift toward a more explosive volcanism. Large volcano-plutonic massifs of syenite and trachyte have hence developed during the last 15 Ma in the south-western province of Kerguelen (Gagnevin et al., 2003). Until recently, the youngest volcanic edifice of the island was thought to be the Mont Ross – the highest summit of Kerguelen – which was active between 1 Ma and 130 ka (Weis et al., 1998).

Lake Armor is located on Kerguelen's main island, 50 km north-east and downwind from the main volcanic edifices on Rallier du Baty Peninsula (Fig. 1). The lake is located 5m asl, is 4 km long and 500 m wide and separated from the sea by a bedrock sill. Bathymetric and seismic surveys were conducted in 2006 and revealed two sub-basins – 100 and 50 m deep – separated by a 20-m-deep rock-sill (Fig. 1), probably of glacial origin (Heirman et al., 2012). A small isolated depocenter on top of this rock-sill records only the air-borne fraction of allochthonous input, whereas the deeper sub-basins record also river-borne sediments, primarily from the main inlet in the north-western end of the lake. Seismic imaging revealed a post-glacial infilling in which 3 units could be recognised (Fig. 1). NW-facing slopes of the central rock-sill seem instable as they are marked by the presence of two underwater landslides.

In 2006, ten short cores were collected from the two main sub-basins, as well as from the small perched depocenter on the sill, using an UWITEC gravity corer. Based on the results of the coring survey and on seismic imagery (Heirman et al., 2012), two sites were selected for

retrieving longer cores. These were taken in 2014 using an UWITEC platform and different piston corers. Despite the particularly harsh weather conditions, several cores were collected on each site (Arnaud et al., 2016), giving the opportunity of choosing the optimal cores for tephrochronology and banking material for further studies. From site I (49,4648°S, 69,7137°E), a modified Nesje-type corer (Nesje, 1992) designed and built up on the field from parts of an UWITEC Usinger-modified piston corer, was used to take the single run 6.1 m long ARM14-I-04 core, which was subsequently split into four sections (S1). From site II (49,45675°S, 69,70193°E), the ARM14-II-03 core was obtained as a composite of a 4 m Nesje-type core (subsequently split into 3 sections), and completed in the same hole by two runs of a 2-m-long UWITEC Niederreiter-type piston corer. Unfortunately, on site II, the sediment below 4 m depth was made of particularly loose non-compacted sand and *ca.* 80 cm were lost at the bottom of each of those runs. The sequence hence reached *ca.* 7.2 m but was fully recovered only down to 4 m, with two additional floating sequences between ca. 4 to 5.1 m and 6 to 7.2 m (S1).

The cores were split into two halves at the EDYTEM laboratory. Each half-section was described in detail and pictures were taken. Lithological description of the sequence allowed the identification of different sedimentary facies.

X-Ray Fluorescence (XRF) core-scanning was performed for the entire composite sequence with a step size of 5 mm and 0.5 mm for ARM14-I and ARM14-II, respectively, using an Avaatech core-scanner (EDYTEM). X-ray were generated with a Rh anode and geochemical data were obtained with two voltage settings: 10 kV and 1 mA for 20 s for Al, Si, S, K, Ca, Ti, Mn, and Fe and 30 kV and 0.75 mA for 30 s for Cu, Zn, Br, Sr, Rb, Zr, and Pb (Richter et al., 2006). Each individual power spectrum was converted by a deconvolution process into relative components (intensities) expressed in counts per second.

Sediment core ARM14-I-04 was then subsampled by slicing every 0.5 to 2 cm, depending on the sedimentary facies, in total 591 samples. The dry bulk density (DBD) of each sample was obtained from difference in weight (wet vs dry) after freeze-drying. The 591 sampled volumes were between 1 and 5.5 cm^3 and densities vary between 0.17 to 1.18 $g.cm^{-3}$. Each sediment slice was then ground (< 63 µm) using agate mortars for further chemical analysis. For each sample, total Hg concentration (THg) was determined by atomic absorption spectrophotometry following dry mineralization and gold amalgamation using an automatic mercury analyzer [Altec, model AMA 254 (Guédron et al. 2009)]. Quality control for THg analysis was performed by periodic measurements of blanks (n=73), certified reference materials [CRMs: IAEA-158 (n=26), NRCC MESS-3 (n=40) and BCR-679 (n=5)], and sample replicates (n=48). The measurement error was 6.2 % on average and always below 10 %. THg was quantified introducing 100 to 200 mg of dry weight sample, leading to a mass of Hg between 0.6 to 40 ng, while the detection limit was 55 pg of Hg (3SD of blank) and the quantification limit was 185 pg of Hg (10SD of blank). The 3 CRMs showed excellent recoveries with values of 128.1 ± 6.2 ng g^{-1} (certified value = 132 ± 14 ng g^{-1}) for IAEA-158, 92.9 ± 2.3 ng g^{-1} (certified value = 91 ± 9 ng g^{-1}) for MESS-3, and 6.9 ±0.6 ng g^{-1} (certified value = 6.3 ± 1.4 ng g^{-1}) for BCR-679. Measurement error on sample replicates ranged from 0.03 to 5.38 %.

Eleven samples of glass shards and pumice layers were selected for major element analysis of glass with an electron microprobe CAMECA© SX100 (Magmas & Volcanoes Laboratory in Clermont-Ferrand, France). Tephra samples were embedded in epoxy resin, polished and carbon metallized. Specific setting for glass analysis was used (low current intensity 5 nA, 15

keV, long count for Na and K- 60 s, and background after peak measurement). Only 8 over the 11 samples yielded statically acceptable results.

Laser Ablation coupled with an ICP-MS was used to analyse the trace and rare earth elements (REE) composition of three samples of glass shards and pumices (also at Magmas & Volcanoes Laboratory in Clermont-Ferrand). The equipment used was an excimer laser system 193 nm Resonetics M-50E, completely computer-controlled and equipped with a laser ATL ultra short pulse duration (< 4 ns), coupled to an ICP-MS spectrometer Agilent 7500 with an optical "cs" high sensitivity and a strengthened pump interface. Reproducibility and accuracy of the analyses was estimated through repeated analyses of BCR-2g standard at the beginning and at the end of each run. Data reduction was carried out with the software package GLITTER (Macquarie Research Ltd, 2001 ; van Achterbergh et al., 2001). For each analysis, the time-resolved signal for each element was monitored to discard perturbations related to inclusions, fractures or mixing.

The upper 10 cm of core ARM14-II were sampled every 5 mm for short-lived radionuclide measurements, using high-efficiency, very low-background, well-type Ge detectors at the Modane Underground Laboratory (LSM) (Reyss et al., 1995). Counting times of 24 to 48 hours were required to reach a statistical error of less than 10 % for excess ^{210}Pb in the deepest samples and for the ^{137}Cs peak. In each sample, the ^{210}Pb excess activities ($^{210}Pb_{ex}$) were calculated by subtracting the ^{226}Ra-supported activity from the total ^{210}Pb activity.

Twelve and 14 samples of plant macro-fossils were taken from ARM14-I and ARM14-II, respectively, for AMS radiocarbon dating. Radiocarbon content was measured at the Laboratoire de Mesure 14C (LMC14) ARTEMIS at the CEA (Atomic Energy Commission) institute at Saclay (samples referenced with the prefix Sac in Tab 1) and at the Poznan Radiocarbon Laboratory (samples referenced with the prefix Poz in Tab 1). Remains of terrestrial plants were preferred, except in core ARM14-I, which did not contain any, and for which radiocarbon dating was done on aquatic plant fragments. However, as there is no carbonate in the catchment, we do not expect any significant reservoir effect. Radiocarbon ages were calibrated using the SHcal04 calibration curve (McCormac et al., 2004). Then, we used “clam” (version 3.0.2), the R-based (R Development Core Team, 2011) algorithm developed by Blaauw (2010), to generate an age/depth model.

3. Results and discussion

3.1. Core description and lithology

On site ARM14-I, the sediment consists of a brownish fine mud (Fig. 2), rich in plant remains. This is consistent with field observations of large bryophytes living at the bottom of the lake in this shallow sub-basin (20 m). The continuous sedimentation is interrupted by nine mineral-rich layers, with grainsize ranges from fine silt up to >1 cm gravels. Seven of those layers contain white mm- to cm-large pumices. The most outstanding feature is a thick pumice layer located between 5.25 and 6.35 m below the lake floor. This layer have an inverse grading, which is typical for sub-aquatic pumice deposits, as larger pumices float better than smaller ones and thus sink later following the pumice rain (e.g. Ikehara, 2015). Visible ash and pumice identified in core ARM14-I were labelled from top to bottom, from A to H. The pumice layer identified at 5 m was labelled H’ as it is not clear, according to the

stratigraphic description, whether it is an individual event or a sub-event following the main pumice-deposit event (H).

Site ARM14-II presents the same facies of continuous sedimentation as ARM14-I, but with a more complex stratigraphy in terms of interbedded deposits. Indeed, in addition to ash and/or pumice layers, several mm- to cm-thick mineral-enriched fine silt layers are also present. Moreover, the number of pumice layers is higher here than in ARM14-I. Because of this complexity it is not straightforward to correlate both sequences. However, two outstanding features can be recognized: i) the uppermost pumice and ash sequence (85-90 cm in ARM14-I; 50-65 cm in ARM14-II), and ii) the lowermost thick and coarse pumice layer. For both features, deposits in ARM14-II appear to be more complex than those in ARM14-I. The higher number of pumice layers in ARM14-II suggests that this site is submitted to sediment remobilisation and re-deposition. Considering the shape of the lake and the available seismic data (Fig. 1), this sediment reworking may originate from the northern flank of the central rock-sill – at the top of which ARM14-I was taken – or from the main river delta (Heirman et al., 2012).

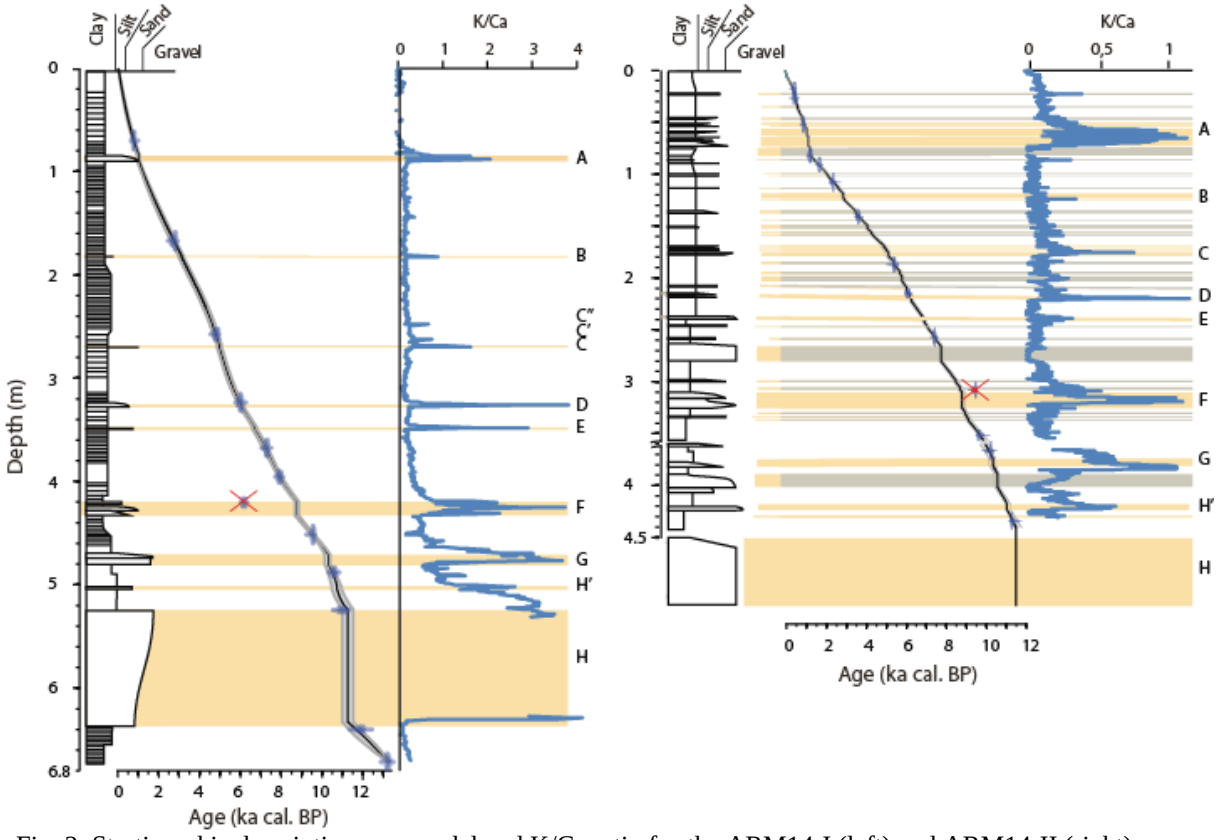

Fig. 2: Stratigraphic description, age model and K/Ca ratio for the ARM14-I (left) and ARM14-II (right) cores. Rejected ^{14}C ages are identified by a red cross, see table 1. Letters on the right part of each panel are identified tephra layers. Yellow stripe highlight layers interpreted as tephra deposits. Grey stripes highlight ARM14-II layers interpreted as *a posteriori* volcanic material reworking.

3.2 Chronology

A logarithmic plot of ($^{210}Pb_{ex}$) activities for ARM14-II (SI2) shows a linearly decreasing trend. According to the constant flux, constant sedimentation rate (CFCS) model (Goldberg, 1963), using the 'serac' R package (Bruel and Sabatier, 2020), the mean accumulation rate is 1.068 ± 0.070 mm.y^{-1} for the upper 10 cm (SI). The profile of ^{137}Cs (SI2) displays an increase

at a depth of 6 cm and a peak between 4 and 5.5 cm. According to other studies from the Southern Hemisphere, the lower peak corresponds to the first appearance of ^{137}Cs at AD 1955, and the upper, peak to AD 1965 (Arnaud et al., 2006; Ficetola et al., 2018). This temporal correlation is supported by the ^{241}Am peak at the same depth, which was a result of the decay of ^{241}Pu in fallout from atmospheric nuclear weapons tests (Appleby, 1991). The good agreement between the ages derived from the $^{210}Pb_{ex}$-CFCS model, and the artificial radionuclide peaks provide a well-constrained, continuous age-depth relationship for the upper 60 cm of ARM14-II (SI2).

Vegetal macro-remains were collected for radiocarbon dating from core ARM14-I (12 samples) and ARM14-II (14 samples) (Table 1). Two radiocarbon ages were excluded, one is to old compared to the others (core ARM14-II), probably due to re-mobilisation and re-deposition of macro-remains stored in the lake catchment area, and the other too young in ARM14-I, possibly caused by contamination during sampling (Fig. 2). Events (=instantaneous sedimentation) such as tephra and reworked layers were removed in both sequences prior to age-depth modelling. The calculated age-depth relationship was done using a smooth spline function using the R-based algorithm "clam" (version 2.2; Blaauw, 2010) with integration of the short-lived radionuclide-derived ages for ARM14-II. This age-depth model was used to date all instantaneous deposits. The vertical bars represent the age of each event thicker than 5 mm with uncertainties (2σ) resulting from the ^{14}C ages (Fig. 2). The first 670 cm of ARM14-I and the first 470 cm of ARM14-II covered the last 13 and 11,5 kyr cal BP, respectively. The event-free sedimentation rate for ARM14-II ranges between 0.16 and 0.83 mm yr^{-1}, with a mean of 0.3 $mm.yr^{-1}$. For ARM14-I the mean event-free sedimentation rate is 0.43 $mm.yr^{-1}$, ranging between 0.14 and 0.83 mm yr^{-1}, below 45 cm sediment depth, and increases to 1,67 $mm.yr^{-1}$ for the upper 45 cm, probably in relation to the higher water content of this organic rich sediment.

Cores	Samples	MCD (m)	Age BP	Age range cal BP
ARM14I	Poz-77362	0,7	800±40	575-744
ARM14I	SacA42461	1,7	2605±30	2497-2757
ARM14I	SacA42462	2,61	4225±30	4584-4838
ARM14I	Poz-77363	3,27	5200±3,15	5752-5995
ARM14I	SacA42463	3,71	6320±35	7028-7294
ARM14I	Poz-77285	4	7030±40	7709-7932
ARM14I	**SacA42464**	**4,25**	**5335±35**	**5943-6188**
ARM14I	SacA42465	4,56	8485±45	9320-9535
ARM14I	SacA42466	4,93	9345±45	10297-10653
ARM14I	Poz-77286	5,32	9580±60	10663-11125
ARM14I	poz- 73369	6,57	10200±50	11503-12029
ARM14I	SacA42467	6,89	11320±50	13056-13256
ARM14II	SacA-12202	0,18	360±30	310-467
ARM14II	SacA-9751	0,263	425±60	317-515
ARM14II	Poz-69603	0,52	970±30	772-918
ARM14II	Poz-69604	0,81	1295±30	1075-1268
ARM14II	Poz-89883	0,91	1775±30	1571-1713
ARM14II	Poz-69605	1,08	2355±35	2181-2455
ARM14II	Poz-69606	1,41	3395±35	3479-3691
ARM14II	Poz-69607	1,87	4680±40	5146-5575
ARM14II	Poz-89884	2,14	5340±40	5941-6203

ARM14II	Poz-89885	2,56	6540±40	7311-7496
ARM14II	**Poz-89887**	**3,06**	**8460±50**	**9304-9528**
ARM14II	Poz-89888	3,51	8720±50	9535-9885
ARM14II	Poz-89889	3,65	9090±50	9941-10373
ARM14II	Poz-89891	4,35	9920±50	11194-11596

Table 1. ^{14}C ages for ARM14I and ARM14II master cores, in bold ages removed for chronology modelling.

3.3. Identification and age of volcanic-related layers

In order to identify more precisely the occurrence of volcanically triggered deposits, both cores were logged on a XRF core scanner. When compared to surrounding basaltic bedrock, Kerguelen most recent volcanic emissions are enriched in potassium (K) relative to calcium (Ca) (Gagnevin et al., 2003), we thus hypothesised that the ratio K/Ca could be a good proxy for the presence of volcanic-triggered layers, as no carbonates are present in the sediment. The XRF-based chemical stratigraphy of ARM14-I confirms this hypothesis, i.e. each tephra layer identified by visual description shows an increase in K/Ca (Figure 2 and 3). Core logging hence led to identify two cryptotephra, which seem to have followed within some decades to centuries the eruption C and further referred as tephra deposits C' and C".

We further used high-resolution mercury (Hg) measurements as an additional conformation for the presence of these tephra deposits (Daga et al., 2016; Guédron et al., 2019; Ribeiro Guevara et al., 2010). During volcanic eruptions, the rapid deposition of massive inorganic volcaniclasts (tephras) results in abrupt drops in the Hg concentration profile (down to 0.9 ng g-1) diluting the uninterrupted organic-rich sediment deposits (average THg = 23.7 ± 6.7 ng g-1) that have accumulated Hg from the atmosphere. For all potential volcanically triggered event deposits (even the cryptotephras C' and C"), the Hg profile depicts a pattern that is mirrored compared to the K/Ca profile, and presents 2 to 20 fold decreases in Hg concentration compared to the baseline value of uninterrupted sedimentation (Fig. 4A).

We further used high-resolution mercury (Hg) measurements as an additional conformation for the presence of these tephra deposits. While volcanoes are a major natural Hg source in the environment through the atmospheric emission of gaseous elemental Hg (Bagnato et al., 2011), during volcanic eruptions the rapid deposition of massive inorganic volcaniclasts (tephras) results in abrupt drops in the local Hg concentration profiles (Daga et al., 2016; Guédron et al., 2019; Ribeiro Guevara et al., 2010). This is the case here with the lowest Hg content measured in tephras (down to 0.9 ng g-1), as compared to the uninterrupted organic-rich sediment deposits (average THg = 23.7 ± 6.7 ng g-1) that have accumulated Hg from the atmosphere. For all potential volcanically triggered event deposits (even the cryptotephras C' and C"), the Hg profile depicts a pattern that is mirrored compared to the K/Ca profile, and presents 2 to 20 fold decreases in Hg concentration compared to the baseline value of uninterrupted sedimentation (Fig. 4A). In a future work, high resolution pre- and post-depositional Hg variations will be discussed thoroughly with geochemical proxies and meteorological factors throughout the entire ARM14-I sediment core.

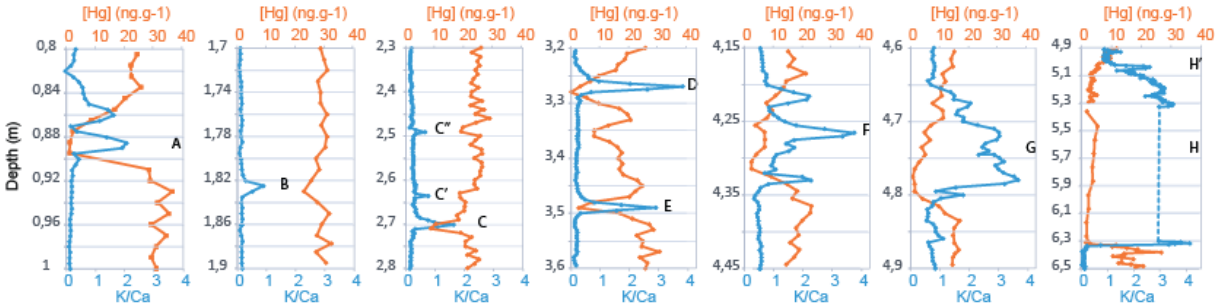

Figure 3. Detection of macro- and cryptotephra deposits using both K/Ca and [Hg] proxies

The chemical stratigraphy combined with independent age-depth models of both cores allowed to determine the event layers that were deposited contemporaneously at both sites (Figures 2 and 3). For this, we applied the following double criterion: i) the presence of a peak in K/Ca, and ii) temporal correlation of similar deposits in both cores. Using this approach, it was possible to correlate all main event deposits in ARM14-I and ARM14-II (Fig. 4). However, in order to assess the intensity of triggering eruptions we used core ARM14-I only because it is solely submitted to direct atmospheric fallout, whereas site II receives input from both direct fallout and river-borne reworked material. Figure 4 shows the thickness of tephra layers and their average grain size.

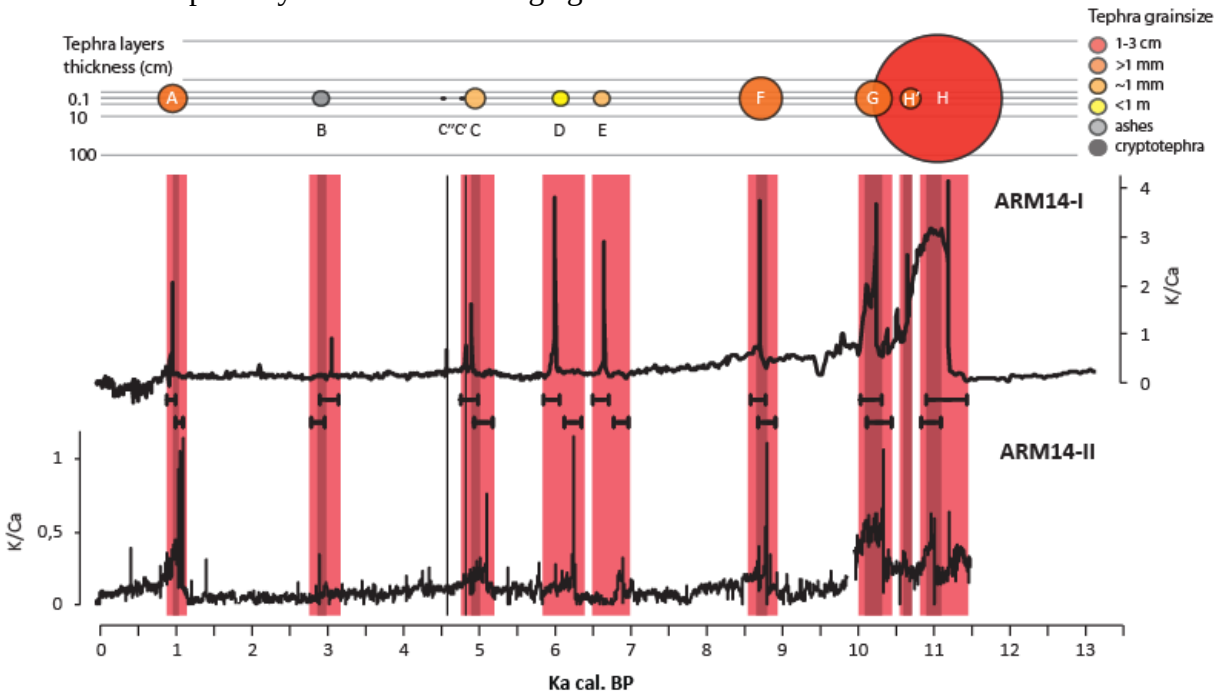

Fig. 4: Synoptic representation of Kerguelen tephrostratigrphy. The upper panel shows the thickness and grainsize of tephra in core ARM14-I. The lower panel displays K/Ca ratios in ARM14-I and ARM14-II in relation to age. Light red bands correspond to age uncertainties and dark red bands represent shared age interval in both cores of each tephra layer.

This analysis leads to the identification of 8 main volcanic eruption events over the last 13,000 years, labelled A to H, from the youngest to the oldest, and 3 smaller events, following shortly after a larger one, labelled C' and C" (following eruption C) and H' (following eruption H). We note a high recurrence of events in the early Holocene: i.e. *ca.* 1 event per millennium. These early Holocene events appear also to have been stronger than subsequent events, as they all produced tephra layers of 1 to 10 cm in thickness. Only four weaker events (all in the thickness range of 0.1 to 1 cm, or below) occurred between 1,000 (layer A) and 8,500 ka cal. BP (layer F), i.e. a mean recurrence interval of 1 event every 2 millennia. The

very last eruption occurred only ca. 1,000 years ago and brought a pumice layer thicker and coarser than any of the eruptions since 8,500 ka cal. BP.

X-Ray Fluorescence (XRF) core-scanning was performed for the entire composite sequence with a step size of 5 mm and 0.5 mm for ARM14-I and ARM14-II, respectively, using an Avaatech core-scanner (EDYTEM). X-ray were generated with a Rh anode and The geochemical data were obtained with two tubetwo voltage settings: 10 kV and 1 mA for 20 s for Al, Si, S, K, Ca, Ti, Mn, and Fe and 30 kV and 0.75 mA for 30 s for Cu, Zn, Br, Sr, Rb, Zr, and Pb (Richter et al., 2006). Each individual power spectrum was converted by a deconvolution process into relative components (intensities) expressed in counts per second.

The oldest event has also been the one yielding the most important amount of pumices to Lake Armor. With more than 1m of deposit without any focusing factor at site I and a maximum pumice size of several centimetres, it is probable that this event that occurred 70km away from our study site has been of extreme explosiveness.

Tephra #		A	B	C''	C'	C	D	E	F	G	H'	H
Depth (cm)	Top	85	178	249	263	268,5	328	348	420	472	510	524,5
	Bottom	90,5	179	249	263	270,5	328	349,5	433,5	481	513	633
Age (cal. BP)	min95%	872	2803	4423	4675	4766	5875	6510	8610	10054	10497	10927
	best	**944**	**2950**	**4559**	**4805**	**4894**	**6003**	**6649**	**8705**	**10246**	**10737**	**11191**
	max95%	998	3045	4680	4913	4999	6087	6726	8796	10333	10995	11457
Thickness (cm)		6	2	<0,1	<0,1	3	1	1,5	13,5	9	3	109
Visual description		> 1 mm pumices	ash layer	cryptotephra	cryptotephra	~1 mm pumices	< 1mm pumices	~1 mm pumices	> 1 mm pumices	> 1 mm pumices	> 1 mm pumices	1-3 cm pumices
Number of microprobe data		3	0	0	4	8	7	0	7	8	7	5
SiO2	%	**64,78**			**64,69**	**62,92**	**64,16**		**64,87**	**64,33**	**65,28**	**64,21**
	+/- 1 sigma	0,47			0,65	1,10	0,55		1,01	1,21	0,87	0,79
TiO2	%	**0,36**			**0,40**	**0,53**	**0,46**		**0,42**	**0,34**	**0,31**	**0,33**
	+/- 1 sigma	0,04			0,06	0,09	0,02		0,07	0,03	0,07	0,03
Al2O3	%	**15,58**			**15,68**	**16,50**	**16,53**		**15,84**	**15,76**	**14,82**	**15,75**
	+/- 1 sigma	0,17			0,75	0,74	0,13		0,89	0,46	1,16	0,34
MgO	%	**0,09**			**0,07**	**0,26**	**0,26**		**0,13**	**0,10**	**0,14**	**0,21**
	+/- 1 sigma	0,02			0,09	0,09	0,04		0,07	0,04	0,10	0,02
FeO	%	**5,04**			**4,61**	**4,94**	**4,38**		**4,79**	**4,45**	**4,79**	**4,52**
	+/- 1 sigma	0,29			0,22	0,45	0,28		0,16	0,12	0,38	0,14
MnO	%	**0,17**			**0,24**	**0,22**	**0,16**		**0,18**	**0,18**	**0,18**	**0,24**
	+/- 1 sigma	0,08			0,13	0,08	0,09		0,12	0,10	0,06	0,06
CaO	%	**0,88**			**0,84**	**1,18**	**1,07**		**0,99**	**0,88**	**0,75**	**0,88**
	+/- 1 sigma	0,06			0,19	0,14	0,02		0,24	0,09	0,22	0,05
Na2O	%	**6,85**			**6,80**	**6,24**	**6,19**		**6,45**	**6,51**	**6,52**	**6,24**
	+/- 1 sigma	0,05			0,32	0,39	0,19		0,33	0,18	0,34	0,22
K2O	%	**5,25**			**5,44**	**5,81**	**5,93**		**5,39**	**5,31**	**5,15**	**5,55**
	+/- 1 sigma	0,13			0,36	0,38	0,12		0,33	0,18	0,48	0,04

Tab. 2. List of trachytic volcanic deposits identified in core ARM14-I, with their depth in the core, estimated age, thickness, visual description and when available, major element concentrations

3.4 Geochemical characterisation and origin of tephra deposits

The geochemical characteristics of the tephra together with the very close proximity of trachytes that were described on Rallier du Baty Peninsula confirms their trachytic origin (Fig. 5A). The hypothesis of a local origin is hence strongly supported. Moreover, the closest landmasses up-wind are the Crozet Archipelago (1300 km) and the Prince Edward Islands (2300 km), which did not produce trachytic volcanism.

Major element analyses indicate that tephra can be attributed to an alkaline silica-saturated magmatic series. The concentrations of $Na_2O + K_2O$ and SiO_2 display a very low variability (Fig 5B). This can be explained, despite an intense fractional crystallization process, by the fact that the trachytic magma has reached the azeotrope of the alkali feldspars and therefore the magmatic liquid has the same composition as anorthose, which crystallizes. Only a change in water activity can allow a change in the major element composition of melts to rhyolitic

magmas. Contrarily, the rare earth element (REE) composition displays a significant variability, illustrating the fractional crystallization process over time in a magma chamber emptied by successive episodes (Fig. 5A). This is well illustrated by a progressive decrease of compatible elements, such as Eu, and an increase of highly incompatible elements as other REE over time.

It is not clear yet if all tephra come from the same volcano and/or the same magma chamber. Indeed, if REEs show an increasing concentration during successive eruptions, this is not the case for major and minor elements (CaO, TiO2) of tephra H, which show distinct compositions. It is quite possible, given the age data already obtained on Rallier du Baty Peninsula (Ethien et al., 2003), that the most recent tephra come from the eruptive centre of Mont Saint-Allouarn in the south of the peninsula and that the tephra H comes from another eruptive centre further north of the peninsula.

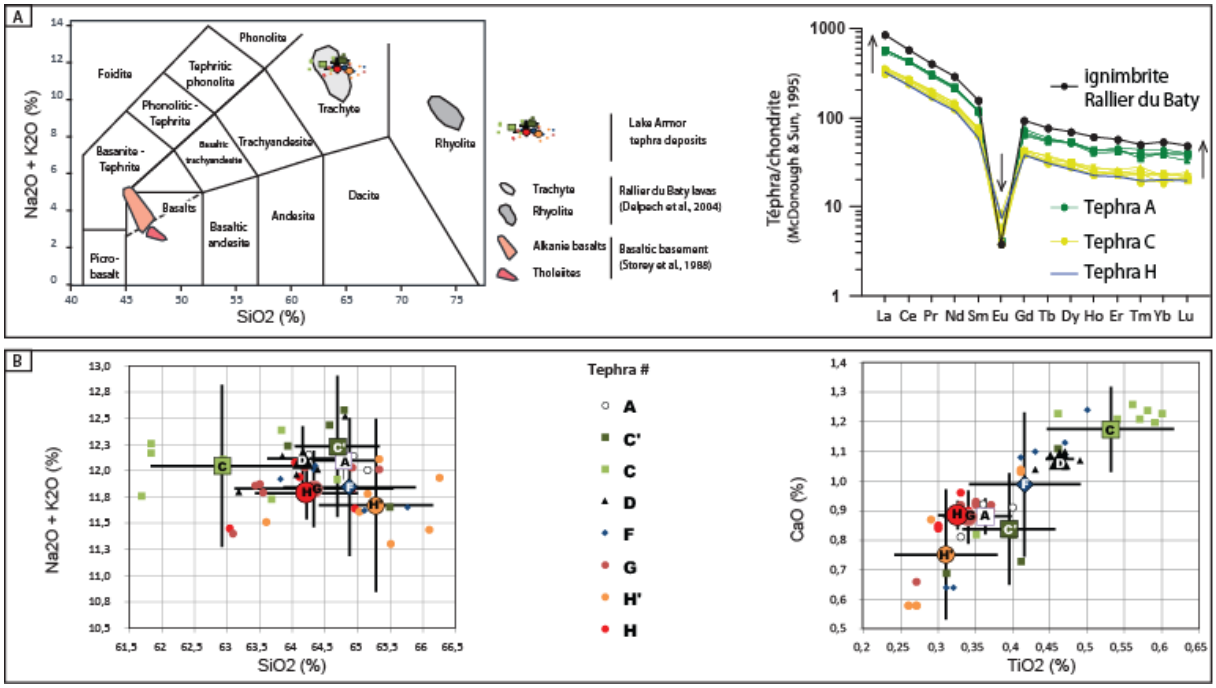

Fig. 5. Geochemical characterisation of Kerguelen tephra deposits. A]

Conclusion

Our first attempt to build a tephrostratigraphic framework for the Kerguelen Archipelago resulted in a list of 8 main Holocene volcanic events (A, B, C, D, E, F, G and H), to which 3 minor events may be added (C', C" and H'). Their geochemical composition, as well as their computed ages are given in Table II. Ongoing studies on cores from several lakes in the Kerguelen Archipelago will benefit from this first framework, and will allow to synchronise the records.

Whereas no evidence of Holocene volcanic activity had previously been published, our results show eight main Holocene volcanic events (A, B, C, D, E, F, G and H) as well as three minor events (C', C" and H') giving a mean return period of one event per millennium. The last eruption occurred ca. 1,000 years ago and was significantly stronger than any of the eruptions during the last 8,500 ka cal. BP. The biggest eruption is also the oldest and occurred close to the onset of the Holocene (11 ka cal. BP). The geochemical composition of the deposits points to a common origin local source at the Rallier-du-Baty Peninsula SW Kerguelen.

Ongoing studies on cores from several lakes in the Kerguelen Archipelago will benefit from this first framework, and will allow robust synchronising of new records.

Acknowledgements

We are warmly grateful to IPEV, the French Polar Institute, for providing necessary logistical support for field expeditions (programmes 448-PEISACG, 444-DyLIOKer, 1094-PALAS). Roland Pagni and Dries Boone are warmly thanked for their help on the field. The authors thank the French CNRS-INSU national coring facility and in particular project ANR-11-EQPX-0009-CLIMCOR, for providing coring facilities. Radiocarbon dates referred as SacA were performed at LMC14 facility in Saclay, in the framework of the national programme ARTEMIS. The authors express their grateful thanks to the LMC14 team, in particular to Jean-Pascal Dumoulin, as well as to Tomas Goslar from Poznan Radioacarbon Laboratory for constant help in the management of ^{14}C samples and results. XRF core scanning was performed thanks at EDYTEM lab as part of the CEMBRO regional analytical facility. The authors thank the Laboratoire Souterrain de Modane (LSM) facilities for the gamma spectrometry measurements and Environnement, Dynamique et Territoires de Montagne (EDYTEM) for the core scanner X-ray fluorescence analyses. This is Laboratory of Excellence ClerVolc contribution n°XXX. The Norwegian contribution was funded by the Norwegian Research Council under the project Shifting Climate States of the Polar Regions (SHIFTS) (project number; 210004).

Appleby, P.G., 1991. 241Am dating of lake sediments. Hydrobiologia 214, 35–42.

Arnaud, F., Fanget, B., Malet, E., Poulenard, J., Eivind, S., Leloup, A., Jostein, B., Sabatier, P., 2016. Extensive lake sediment coring survey on Sub-Antarctic Indian Ocean Kerguelen Archipelago (French Austral and Antarctic Lands), in: Geophysical Research Abstracts. Presented at the EGU General Assembly 2016, EGU, Vienne, Autriche, p. 12876.

Arnaud, F., Magand, O., Chapron, E., Bertrand, S., Boës, X., Charlet, F., Mélières, M.-A., 2006. Radionuclide dating (210Pb, 137Cs, 241Am) of recent lake sediments in a highly active geodynamic setting (Lakes Puyehue and Icalma—Chilean Lake District). Sci. Total Environ. 366, 837–850. https://doi.org/10.1016/j.scitotenv.2005.08.013

Arnaud, F., Révillon, S., Debret, M., Revel, M., Chapron, E., Jacob, J., Giguet-Covex, C., Poulenard, J., Magny, M., 2012. Lake Bourget regional erosion patterns reconstruction reveals Holocene NW European Alps soil evolution and paleohydrology. Quat. Sci. Rev. 51, 81–92. https://doi.org/10.1016/j.quascirev.2012.07.025

Bagnato, E., Aiuppa, A., Parello, F., Allard, P., Shinohara, H., Liuzzo, M., Giudice, G., 2011. New clues on the contribution of Earth's volcanism to the global mercury cycle. Bull. Volcanol. 73, 497–510. https://doi.org/10.1007/s00445-010-0419-y

Blaauw, M., 2010. Methods and code for 'classical' age-modelling of radiocarbon sequences. Quat. Geochronol. 5, 512–518.

Bruel, R., Sabatier, P., 2020. serac: a R package for ShortlivEd RAdionuclide Chronology of recent sediment cores (preprint). EarthArXiv. https://doi.org/10.31223/osf.io/f4yma

Daga, R., Ribeiro Guevara, S., Pavlin, M., Rizzo, A., Lojen, S., Vreča, P., Horvat, M., Arribére, M., 2016. Historical records of mercury in southern latitudes over 1600years: Lake Futalaufquen, Northern Patagonia. Sci. Total Environ. 553, 541–550. https://doi.org/10.1016/j.scitotenv.2016.02.114

Dahl, S.O., Bakke, J., Lie, Ø., Nesje, A., 2003. Reconstruction of former glacier equilibrium-line altitudes based on proglacial sites: an evaluation of approaches and selection of sites. Quat. Sci. Rev. 22, 275–287. https://doi.org/10.1016/S0277-3791(02)00135-X

Debret, M., Chapron, E., Desmet, M., Rolland-Revel, M., Magand, O., Trentesaux, A., Bout-Roumazeille, V., Nomade, J., Arnaud, F., 2010. North western Alps Holocene paleohydrology recorded by flooding activity in Lake Le Bourget, France. Quat. Sci. Rev. 29, 2185–2200. https://doi.org/10.1016/j.quascirev.2010.05.016

Ethien, R., Feraud, G., Gerbe, M.C., Cottin, J.Y., O'Reilly, S.Y., Giret, A., 2003. Geochemistry and Ar/Ar dating of upper pleistocene volcanic rocks from Kerguelen islands (Indian Ocean). Presented at the EGS - AGU - EUG Joint Assembly, p. 6432.

Ficetola, G.F., Poulenard, J., Sabatier, P., Messager, E., Gielly, L., Leloup, A., Etienne, D., Bakke, J., Malet, E., Fanget, B., Støren, E., Reyss, J.-L., Taberlet, P., Arnaud, F., 2018. DNA from lake sediments reveals long-term ecosystem changes after a biological invasion. Sci. Adv. 4, eaar4292. https://doi.org/10.1126/sciadv.aar4292

Fontijn, K., Rawson, H., Van Daele, M., Moernaut, J., Abarzúa, A.M., Heirman, K., Bertrand, S., Pyle, D.M., Mather, T.A., De Batist, M., Naranjo, J.-A., Moreno, H., 2016. Synchronisation of sedimentary records using tephra: A postglacial tephrochronological model for the Chilean Lake District. Quat. Sci. Rev. 137, 234–254. https://doi.org/10.1016/j.quascirev.2016.02.015

Gagnevin, D., Ethien, R., Bonin, B., Moine, B., Féraud, G., Gerbe, M.C., Cottin, J.Y., Michon, G., Tourpin, S., Mamias, G., Perrache, C., Giret, A., 2003. Open-system processes in the genesis of silica-oversaturated alkaline rocks of the Rallier-du-Baty Peninsula, Kerguelen Archipelago (Indian Ocean). J. Volcanol. Geotherm. Res. 123, 267–300. https://doi.org/10.1016/S0377-0273(02)00509-7

Goldberg, E.D., 1963. Geochronology with 210Pb, in: Radioactive Dating. pp. 121–131.

Guédron, S., Tolu, J., Brisset, E., Sabatier, P., Perrot, V., Bouchet, S., Develle, A.L., Bindler, R., Cossa, D., Fritz, S.C., Baker, P.A., 2019. Late Holocene volcanic and anthropogenic mercury deposition in the western Central Andes (Lake Chungará, Chile). Sci. Total Environ. 662, 903–914. https://doi.org/10.1016/j.scitotenv.2019.01.294

Heirman, K., De Batist, M., Arnaud, F., De Beaulieu, J.-L., 2012. Seismic stratigraphy of the late Quaternary sedimentary infill of Lac d'Armor (Kerguelen archipelago): a record of glacier retreat, sedimentary mass wasting and southern Westerly intensification. Antarct. Sci. 24, 608–618. https://doi.org/10.1017/S0954102012000466

Ikehara, K., 2015. Marine tephra in the Japan Sea sediments as a tool for paleoceanography and paleoclimatology. Prog. Earth Planet. Sci. 2, 36. https://doi.org/10.1186/s40645-015-0068-z

McCormac, F.G., Hogg, A.G., Blackwell, P.G., Buck, C.E., Higham, T.F.G., Reimer, P.J., 2004. Shcal04 Southern Hemisphere Calibration, 0–11.0 Cal Kyr BP. Radiocarbon 46, 1087–1092. https://doi.org/10.1017/S0033822200033014

Nesje, A., 1992. A Piston Corer for Lacustrine and Marine Sediments. Arct. Alp. Res. 24, 257. https://doi.org/10.2307/1551667

Oppedal, Bilt, W.G.M. van der, Balascio, N.L., Bakke, J., 2018. Patagonian ash on sub-Antarctic South Georgia: expanding the tephrostratigraphy of southern South America into the Atlantic sector of the Southern Ocean. J. Quat. Sci. 33, 482–486. https://doi.org/10.1002/jqs.3035

Oppedal, L.T., Bakke, J., Paasche, Ø., Werner, J.P., van der Bilt, W.G.M., 2018. Cirque Glacier on South Georgia Shows Centennial Variability over the Last 7000 Years. Front. Earth Sci. 6, 2. https://doi.org/10.3389/feart.2018.00002

Peterse, F., Vonk, J.E., Holmes, R.M., Giosan, L., Zimov, N., Eglinton, T.I., 2014. Branched glycerol dialkyl glycerol tetraethers in Arctic lake sediments: Sources and implications for paleothermometry at high latitudes. J. Geophys. Res. Biogeosciences 119, 1738–1754. https://doi.org/10.1002/2014JG002639

R Development Core Team, 2011. R: a Language and Environment for Statistical Computing. R Foundation for Statistical Computing, Vienna.

Reyss, J.-L., Schmidt, S., Legeleux, F., Bonte, P., 1995. Large low background well type detectors for measurements of environmental radioactivity. Nucl Instrum Methods 357, 391–397.

Ribeiro Guevara, S., Meili, M., Rizzo, A., Daga, R., Arribére, M., 2010. Sediment records of highly variable mercury inputs to mountain lakes in Patagonia during the past millennium. Atmospheric Chem. Phys. 10, 3443–3453. https://doi.org/10.5194/acp-10-3443-2010

Roche-Bellair, N., 1976. Les variations climatiques de l'holocène supérieur des îles Kerguelen: d'après la coupe d'une tourbière de la plaine de Dante (côte méridionale). Comptes Rendus Académie Sci. Sér. D 282, 1257–1260.

Saunders, K.M., Roberts, S.J., Perren, B., Butz, C., Sime, L., Davies, S., Van Nieuwenhuyze, W., Grosjean, M., Hodgson, D.A., 2018. Holocene dynamics of the Southern Hemisphere westerly winds and possible links to CO2 outgassing. Nat. Geosci. https://doi.org/10.1038/s41561-018-0186-5

Shulmeister, J., Goodwin, I., Renwick, J., Harle, K., Armand, L., McGlone, M.S., Cook, E., Dodson, J., Hesse, P.P., Mayewski, P., Curran, M., 2004. The Southern Hemisphere westerlies in the Australasian sector over the last glacial cycle: a synthesis. Quat. Int., Climates, human, and natural system of the PEPII transect 118–119, 23–53. https://doi.org/10.1016/S1040-6182(03)00129-0

Sijp, W.P., England, M.H., 2009. Southern Hemisphere Westerly Wind Control over the Ocean's Thermohaline Circulation. J. Clim. 22, 1277–1286. https://doi.org/10.1175/2008JCLI2310.1

van Achterbergh, E., Griffin, W.L., Stiefenhofer, J., 2001. Metasomatism in mantle xenoliths from the Letlhakane kimberlites: estimation of element fluxes. Contrib. Mineral. Petrol. 141, 397–414. https://doi.org/10.1007/s004100000236

van der Bilt, W.G.M., Bakke, J., Werner, J.P., Paasche, Ø., Rosqvist, G., Vatle, S.S., 2017. Late Holocene glacier reconstruction reveals retreat behind present limits and two-stage Little Ice Age on subantarctic South Georgia. J. Quat. Sci. 32, 888–901. https://doi.org/10.1002/jqs.2937

Van der Putten, N., Hébrard, J.-P., Verbruggen, C., Van de Vijver, B., Disnar, J.-R., Spassov, S., de Beaulieu, J.-L., De Dapper, M., Keravis, D., Hus, J., Thouveny, N., Frenot, Y., 2008. An integrated palaeoenvironmental investigation of a 6200 year old peat sequence from Ile de la Possession, Iles Crozet, sub-Antarctica. Palaeogeogr. Palaeoclimatol. Palaeoecol. 270, 179–195. https://doi.org/10.1016/j.palaeo.2008.09.014

Van der Putten, N., Stieperaere, H., Verbruggen, C., Ochyra, R., 2004. Holocene palaeoecology and climate history of South Georgia (sub-Antarctica) based on a macrofossil record of bryophytes and seeds. The Holocene 14, 382–392. https://doi.org/10.1191/0959683604hl714rp

Van der Putten, N., Verbruggen, C., Björck, S., Michel, E., Disnar, J.-R., Chapron, E., Moine, B.N., de Beaulieu, J.-L., 2015. The Last Termination in the South Indian Ocean: A unique terrestrial record from Kerguelen Islands (49°S) situated within the Southern Hemisphere westerly belt. Quat. Sci. Rev. 122, 142–157. https://doi.org/10.1016/j.quascirev.2015.05.010

Weis, D., Frey, F.A., Giret, A., Cantagrel, J.-M., 1998. Geochemical Characteristics of the Youngest Volcano (Mount Ross) in the Kerguelen Archipelago: Inferences for Magma Flux, Lithosphere Assimilation and Composition of the Kerguelen Plume. J. Petrol. 39, 973–994. https://doi.org/10.1093/petroj/39.5.973

Wessels, M., 1998. Natural environmental changes indicated by Late Glacial and Holocene sediments from Lake Constance, Germany. Palaeogeogr. Palaeoclimatol. Palaeoecol. 140, 421–432. https://doi.org/10.1016/S0031-0182(98)00026-1

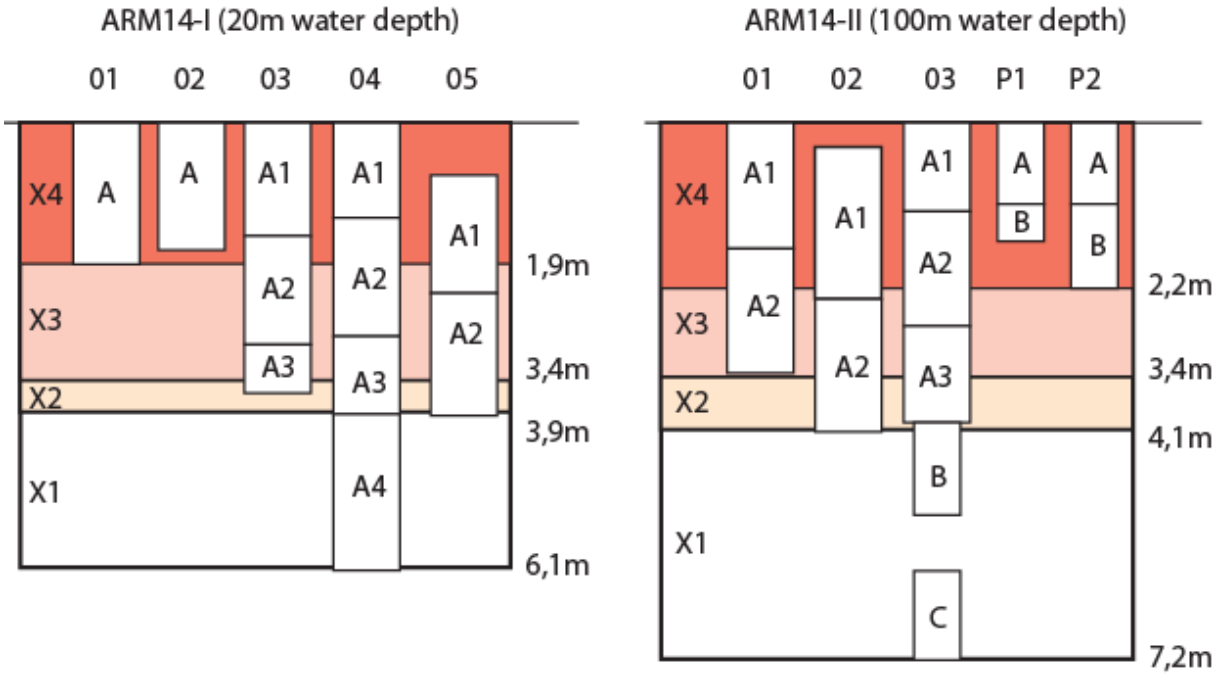

S1. Scheme of different core sections taken in Lake Armor site 14-I (perched basin) and 14-II (deep basin) during the 2014 PALAS expedition. Background colours reflect the number of sections available for a given depth, from 4 (X4) to 1 (X1). NB: those depths correspond to measurements makes on the field, due to further decompression of the sediment, they are slightly different from model-depths used while referring sample depths in the paper.

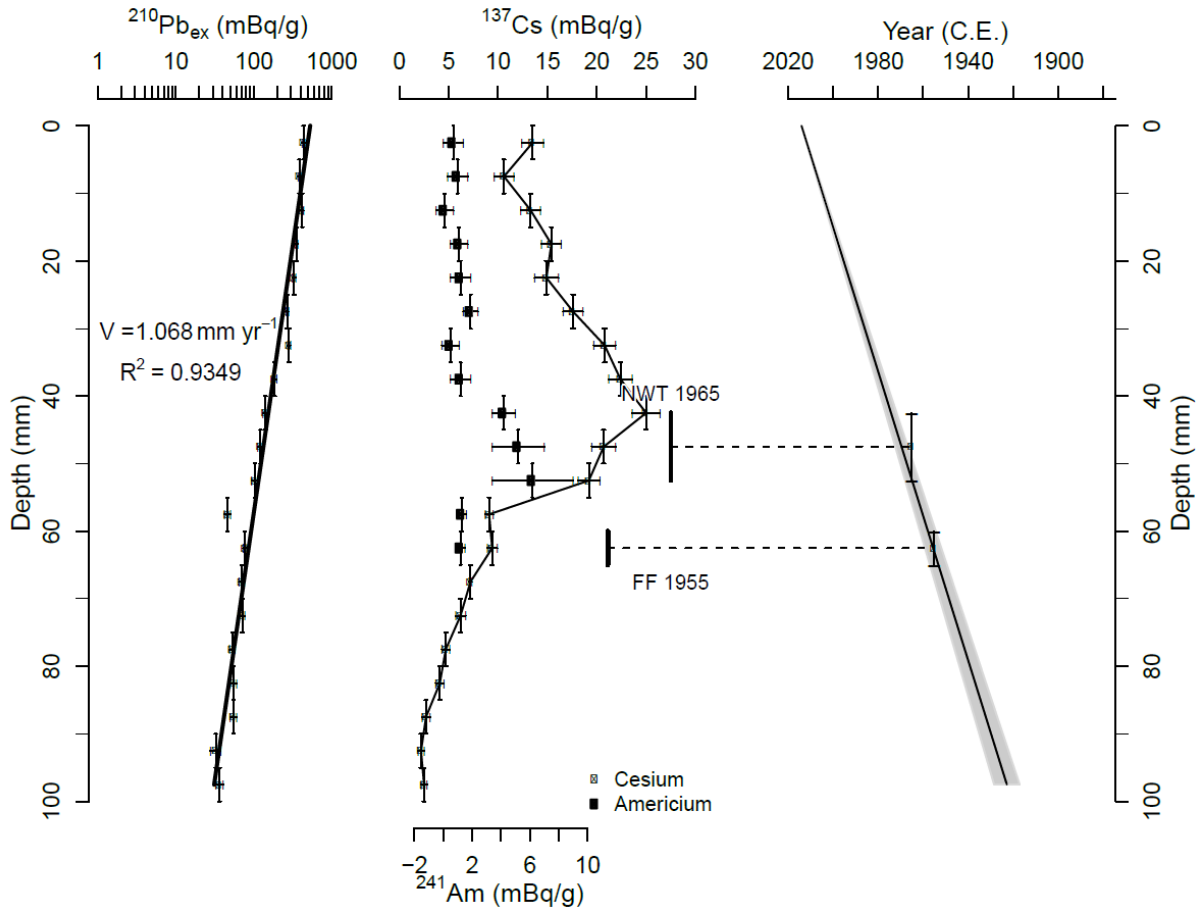

Figure S2 : From left to right : ^{210}Pbex activities, ^{137}Cs and ^{241}Am activities, and the age model for the upper 10 cm of ARM14 II computed thanks to *serac* R package (Bruel and Sabatier, 2020).